Primary carbide transformation in a high performance micro-alloy at 1000 °C

Wang, Minshi; Flahaut, Dominque; zhang, zhu; Jones, Ian; Chiu, Yu-Lung

DOI:
10.1016/j.jallcom.2018.12.095
10.1016/j.jallcom.2018.12.095

Document Version
Peer reviewed version

Citation for published version (Harvard):
Wang, M, Flahaut, D, zhang, Z, Jones, I & Chiu, Y-L 2019, 'Primary carbide transformation in a high performance micro-alloy at 1000 °C', *Journal of Alloys and Compounds*, vol. 781, pp. 751-760. https://doi.org/10.1016/j.jallcom.2018.12.095, https://doi.org/10.1016/j.jallcom.2018.12.095

Primary carbide transformation in a high performance micro-alloy at 1000 oC

Wang, Minshi; Flahaut, Dominque; zhang, zhu; Jones, Ian; Chiu, Yu-Lung

Primary carbide transformation in a high performance micro-alloy at 1000 ^{o}C

Minshi Wang[a], Dominique Flahaut[b], Zhu Zhang[c], Ian P. Jones[a], Yu Lung Chiu[a*]

[a]*School of Metallurgy and Materials, University of Birmingham, Edgbaston, Birmingham B15 2TT, UK*

[b]*Doncasters Paralloy Ltd., Paralloy House, Nuffield Road, TS23 4DA, UK.*

[c]*Doncasters Technical Centre, George Baylis Road, Worcestershire, WR9 9RB, UK*

* *y.chiu@bham.ac.uk*

Abstract

The transformation from $M_7C_3 \rightarrow M_{23}C_6$ in a high performance micro alloy (HP-MA) was studied using different techniques. Following the cooling during the centrifugal casting, the as-cast HP-MA alloy consists of an austenitic matrix with the primary carbide network consisting of a combination of M_7C_3 (M being mainly chromium) and MC (M being mainly niobium). During the heat treatment at 1000 ^{o}C, the primary chromium carbides transform from M_7C_3 to $M_{23}C_6$. The incompletely transformed primary carbide consists of an outer shell of $M_{23}C_6$ carbide (coherent with the austenitic matrix) and a core of M_7C_3 type carbide. The experimentally determined $M_{23}C_6$ shell thickness agrees reasonably well with the estimated diffusion distance of carbon in $M_{23}C_6$ based on Zener's relation implying that the $M_7C_3 \rightarrow M_{23}C_6$ transformation is mainly controlled by the diffusion of the carbon from M_7C_3 to the matrix through the $M_{23}C_6$ shell. This mechanism is discussed vis-à-vis the literature reported mechanism on the transformation.

Introduction

Steam reforming is the main hydrogen production method, currently 50 % of global hydrogen production [1-6]. With the continuous technological improvement throughout the last 70 years [7-11], a new grade of austenitic stainless steel, HP40 (25 % Cr and 35 % Ni), has been developed for the steam reforming process. The most popular material used in steam reforming is HP Micro Alloy (HP-MA), a new micro-alloyed steel with additions of Ti (precipitation strengthening) [12], Nb (high temperature structural stability and grain boundary anti-sliding performance) [13], W (solid solution strengthening) [14] or rare earth elements (to improve high temperature oxidation resistance) [15, 16].

The high chromium (Cr) content in the steel is designed to improve the corrosion resistance by forming a very thin stable Cr-based oxide film on the surface [17]. Meanwhile, the addition of Cr introduces various Cr-containing carbides into the steel, such as M_7C_3 and $M_{23}C_6$ [18, 19], which improves the mechanical properties of the steel by precipitation strengthening. $M_{23}C_6$ is thermodynamically the most stable among these Cr-containing carbides [20] and nucleates intergranularly [21-23] and also intragranularly on defects such as dislocations [24] and twins [25]. In the as-cast condition after the solidification, M_7C_3 presents and transforms into $M_{23}C_6$ upon the heating during service in HP-MA [15, 26-28] and other steels [29, 30]. The $M_7C_3 \rightarrow M_{23}C_6$ transformation and its effect on the mechanical properties of steels have been studied. Vardavoulias et al. [31] found that the fracture mechanism of a cast ferritic stainless steel changed from transgranular cleavage to interdendritic due to the formation of a continuous carbide network associated with the $M_7C_3 \rightarrow M_{23}C_6$ transformation. M_7C_3-austensite eutectic was observed in a 30 wt% Cr cast iron and the eutectic M_7C_3 transformed into $M_{23}C_6$ [32]. Jiang et al. [33] suggested that the decomposition of M_7C_3, which acts as a carbon reservoir, could promote $M_{23}C_6$ precipitation. The orientation relationship between M_7C_3 and $M_{23}C_6$ was identified by Inoue and Masumoto [34], i.e. $(001)_{M_7C_3} \parallel (\bar{1}2\bar{1})_{M_{23}C_6}$. Recently, Wieczerzak et al. [35] determined the effect of heat treatment on the evolution of carbides in a Fe-25Cr-0.8C alloy and found that the $M_7C_3 \rightarrow M_{23}C_6$ transformation occurred at temperatures between

500 and 600 °C. However, the detailed process of $M_7C_3 \rightarrow M_{23}C_6$ transformation in stainless steel has not been reported. The current investigation aims to characterise the nature of the carbides in the as-cast condition and after heat treatment at 1000 °C and to understand the mechanism of $M_7C_3 \rightarrow M_{23}C_6$ transformation.

Materials and experimental procedure

The HP-MA steel used in this study was supplied by Doncasters Paralloy Ltd. The chemical composition of HP-MA was determined by optical emission spectrometry (OES) and is shown in Table 1. Cross-sections through the tubes were prepared for microstructural observation (as-cast HP-MA) and after heat treatment (HT HP-MA). Figure 1 shows a section of an as-cast steel tube. The microstructural observations were performed at locations about 3 mm away from the outer surface (as indicated by the two dashed lines). Heat treatments at 1000 °C for 1, 3, 5, 7 and 9 hours were carried out. For example, HT-1 indicates that the specimen was held at 1000 °C for 1 hour. After holding for the designated time, the specimens were quenched into water.

For microstructural observation, the specimens were mechanically ground and polished down to 0.25 μm. A TESCAN MIRA-3 scanning electron microscope (SEM) equipped with an Oxford Instruments XMax silicon drift detector (SDD) for energy dispersive X-ray spectroscopy (EDS) and an electron backscattered diffraction (EBSD) system, was used for the microstructural characterisation and chemical analysis at 20 kV. Foils for transmission electron microscopy (TEM) were prepared by twin-jet electro-polishing using a solution containing 20% perchloric acid and 80% methanol at 0 °C. A focused ion beam scanning electron microscope (FIB/SEM, FEI Quanta 3D FEG) was also used to prepare TEM specimens from specific positions. TEM examination was performed on a JEM-2100 TEM operated at 200 kV. Scanning transmission electron microscopy (STEM) and EDS analysis were performed on a Philips Tecnai F20 equipped with an Oxford Instruments XMax SDD. X-ray diffraction (XRD) was carried out on a Philips D62-WSC X-ray diffractometer operated at 40 kV and 40 mA with the 2θ scan range of 20-100° and the scan rate of 1°/second using Cu-K_α radiation

(λ=1.541Å). JMat Pro 6.2, a commercial software utilizing core minimization routines developed for the PMLFKT program, was used for the thermodynamic calculations using the TCNI7 database.

Results

Figure 2 (a) shows a back-scattered electron (BSE) image obtained from the as-cast HP-MA sample. Dark and bright particles form a fragmented network around each dendrite. The dark particles are of mixed granular and acicular type, which is described as the eutectic structure and most of the bright particles have a rod-like morphology. From the EDS results (Table 2), the particles in bright contrast correspond to (Nb, Ti)-rich primary carbides while the dark particles correspond to Cr-rich primary carbides. Furthermore, Nb and Ti are confined to the primary carbide network, whereas Si remains in the Fe and Ni-rich matrix. Cr appears to be in the matrix and the primary carbides. XRD analysis confirms that the primary carbides are of M_7C_3 and MC type (Figure 2 (b)). Depletion of Cr was also found close to the Cr-rich primary carbide (Figures 2 (c)&(d)). No precipitation has been observed in the matrix of the as-cast sample. An orientation relationship between M_7C_3 carbide and the austenite matrix ($(100)_{M_7C_3} \parallel (\overline{1}\overline{1}1)_\gamma$) was observed by Ernst et al. [36] in AISI 316L stainless steel. However, this specific orientation relationship between M_7C_3 and austenite was not found in the current work. More than twenty primary Cr-carbide were analysed using EBSD and no particular orientation relationship was found between M_7C_3 carbides and the austenite matrix.

After heat treatment at 1000 ^{o}C, secondary carbides were observed within the matrix close to the primary carbides (as shown in Figure 3). Although the morphology of the primary carbides shows no significant difference as a result of the heat treatment, the Cr-rich primary carbides changed from a homogeneous shade in the as-cast condition (Figure 4 (a)) into two grey levels after the heat treatments (Figure 4 (b-f)). Figure 5(a) illustrates a BSE image of a large Cr-carbide obtained from a HT-5 HP-MA sample showing a core/shell contrast. EBSD analysis (Figure 5b) of the carbide confirms that the outside shell is of $M_{23}C_6$ type and that the core is of M_7C_3 type. Meanwhile, the

colour coded orientation map (Figure 5 (c)) shows that the $M_{23}C_6$ has the same orientation as the austenite matrix. Figure 6(a) shows an SEM image of primary carbides in the HT-5 HP-MA sample. The EBSD phase map in Figure 6(b) shows that the core-shell structure of the M_7C_3 and $M_{23}C_6$. The orientation map in Figure 6(c) shows that although the M_7C_3 carbides have different crystallographic orientations, the $M_{23}C_6$ carbides formed the same orientation as that of the matrix.

A Cr-rich primary carbide in HT-5 HP-MA (Figure 7 (a)) was selected for TEM specimen preparation using the FIB. A TEM bright field image of the FIB-TEM specimen cut from the selected carbide is shown in Figure 7 (b). The SAD patterns obtained confirm that the M_7C_3 (Figure 7 (c)) is surrounded by a shell of $M_{23}C_6$ (Figure 7 (d)). The specific orientation relationship between M_7C_3 and $M_{23}C_6$ in Figure 7 was determined as $(1\bar{1}0)_{M_7C_3} \parallel (1\bar{3}1)_{M_{23}C_6}$ and $[001]_{M_7C_3} \parallel [\bar{1}02]_{M_{23}C_6}$. Some particles of about 20 nm size (Figure 7 (e)) and rich in Ni (Figure 7 (f)&(g)) were observed in the M_7C_3 carbide. Furthermore, Nb-rich particles (Figure 7 (h)) were found at the interface between the $M_{23}C_6$ and the matrix. A MnS particle was also found as shown in Figure 7 (i) and (j), probably from contamination during casting. Figure 7(k) clearly shows that the concentration of carbon is the highest in M_7C_3 followed by that in $M_{23}C_6$ and the lowest in the surrounding matrix. The Cr map (Figure 7(l)) shows not much difference between M_7C_3 and $M_{23}C_6$. Figure 7 (m) and (n) illustrate that $M_{23}C_6$ contains more Fe and Ni than M_7C_3. The TEM EDS results are consistent with the SEM measurement shown in Table 2.

Discussion

As shown in Table 1, the HP-MA contains 0.41 wt% carbon. However, the solubility of carbon in HP-MA austenitic matrix at 1000 ^{o}C is 0.021 wt%, which is given by thermodynamic calculation via JMat Pro. It is obvious that the solubility of carbon in austenite (0.021 wt%) is much smaller than the carbon content in the HP-MA (ie. 0.41 wt%). The solidification to room temperature during casting would lead to the formation of a carbide network, which is in agreement with the

observations in as-cast HP-MA. Although M_7C_3 (30 at%) contains more carbon than $M_{23}C_6$ (21 at%), M_7C_3 can form at low carbon level and similarly $M_{23}C_6$ can form at very high carbon level when chromium content is high enough [37-39]. Gregolin and Alcantara [39] developed a solidification model for Fe-14.7wt%Cr-1.0wt%Nb-2.1wt%C alloys, where MC is the first phase to form when cooled from the liquid (Nb and Ti are strong carbide formers [41]), and the presence of MC is followed by the reaction $L \rightarrow \gamma + M_7C_3$ leading to a eutectic structure. Previous study on Fe-25wt%Cr-5wt%Mo-0.82wt%C [42] also confirmed that a greater thermal gradient at solidification promotes the precipitation of M_7C_3 carbide instead of $M_{23}C_6$, which is related to the short time available for redistribution of carbide forming elements. The same eutectic structure was found in the as-cast HP-MA as shown in Figure 2 (a), indicating that the reaction $L \rightarrow \gamma + M_7C_3$ also occurred during the solidification of HP-MA.

A thermodynamic simulation using JMat Pro was performed and the result is shown in Figure 8. There is one main difference between the results of Gregolin and Alcantara and the current simulation: here the austenite forms in the liquid before MC. As predicted by the simulation, the solidification sequence of HP-MA alloys during equilibrium cooling is therefore:

$$\boldsymbol{L \rightarrow L + \gamma \rightarrow L + \gamma + MC \rightarrow L + \gamma + MC + M_7C_3 \rightarrow \gamma + MC + M_7C_3}$$

$$\uparrow \qquad \uparrow \qquad \uparrow$$

$$\boldsymbol{\gamma \qquad MC \qquad L \rightarrow \gamma + M_7C_3}$$

The first solid state precipitation is of MC. As the temperature decreases further, the reaction $L \rightarrow \gamma + M_7C_3$ would occur yielding the characteristic eutectic structure. The as-cast microstructure of HP-MA therefore consists of austenitic matrix surrounded by primary M_7C_3 and primary MC, which form a fragmented network. The formation of primary Cr-carbides in as-cast HP-MA leads to the chromium depletion in the vicinity of carbides [43-45], as shown in Figure 2 (d).

Although the formation of MC carbide drastically reduces the matrix carbon content, some carbon remains available for later secondary carbide formation during the subsequent heat treatment.

148 The minimum niobium content required to scavenge all the carbon is normally eight times the carbon
149 content [46]. In the HP-MA steel, the concentration of niobium is 1.39 wt% and that of carbon is 0.41
150 wt%, i.e. leaving about 0.24 wt% of the carbon unreacted. Therefore, when the HP-MA alloy was held
151 at 1000 ^{o}C, the available carbon combined with the Cr in the austenite matrix to form the Cr-rich
152 secondary carbide, which is of $M_{23}C_6$ type due to its higher thermodynamic stability than that of M_7C_3
153 [47]. The MC carbides remain stable during the heat treatment in this study. However, MC carbides
154 are no longer stable and will transform into the G-phase ($Ni_{16}Nb_6Si_7$) after long exposure to high
155 temperatures [12, 16, 48, 49].

156 BSE images, EBSD mapping and TEM analysis confirm the transformation of the Cr-rich
157 primary carbide from M_7C_3 to $M_{23}C_6$ during the heat treatment. The incompletely transformed primary
158 carbide consists of an outside shell of $M_{23}C_6$ type carbide and a core of M_7C_3 type carbide. Kaneko et
159 al. [50] found by *in situ* TEM observation that $M_{23}C_6$ carbides which nucleated on grain boundaries
160 have a cube-cube relationship with one of the grains. This preference for one grain, which minimizes
161 the activation energy for nucleation, was also confirmed by Hong et al. [51] in AISI 304 austenitic
162 stainless steel. From Figures 5 and 6, all $M_{23}C_6$ carbides have the same orientation as the matrix. Thus,
163 at the beginning of the $M_7C_3 \rightarrow M_{23}C_6$ transformation, $M_{23}C_6$ carbide coherent with the matrix
164 austenite forms at the carbide/matrix interface and gradually grows into the parent M_7C_3 carbide. This
165 is consistent with the study by Inoue and Masumoto [34] who postulated that the $M_7C_3 \rightarrow M_{23}C_6$
166 transformation could be controlled by the alloying elements diffusing from the matrix to the resultant
167 carbides or carbon diffusion from existing carbides to the matrix. While the diffusion of Cr from the
168 surrounding matrix into carbides has been proposed to explain the observed carbide lattice parameter
169 increase upon heat-treatments, in these cases there was no $M_7C_3 \rightarrow M_{23}C_6$ transformation [53-56]. The
170 lattice parameter increase was attributed to the replacement of Fe atoms by larger Cr atom [52].
171
172 More recently, Wieczerzak et al. [35] studied the $M_7C_3 \rightarrow M_{23}C_6$ transformation in an Fe-Cr-
173 C ternary alloy using in-situ X-ray diffraction within the temperature range from 100 ^{o}C up to 800 ^{o}C.

They observed the lattice parameters of M_7C_3 carbide formed in the as-cast state increased much faster than expected at the temperature range between 400 ^{o}C and 550 ^{o}C. This was attributed to the intensified replacement of Fe atoms in M_7C_3 by Cr atoms from the matrix. This uphill diffusion of Cr from the matrix into the M_7C_3 was claimed to form an energetically more favourable carbide (i.e. $M_{23}C_6$).

However the driving force for the proposed chromium uphill diffusion from matrix into M_7C_3, which is needed if the $M_7C_3 \rightarrow M_{23}C_6$ transformation were controlled by the chromium, remains unclear. To allow Cr diffuses from the matrix into M_7C_3 would need to overcome the extra energy barrier, as it is an uphill chemical diffusion. The lattice constants of the M_7C_3 carbide increase with any uphill-diffused Cr would be expected to further restrict the diffusion of Cr into M_7C_3 due to the strain energy associated with the lattice expansion. In addition, the Cr uphill diffusion controlled $M_7C_3 \rightarrow M_{23}C_6$ transformation would be expected to introduce a significant primary carbide volume change and therefore result in a large strain energy during the transformation. As a crude estimate of the primary carbide volume change upon the $M_7C_3 \rightarrow M_{23}C_6$ transformation, one can simplify that Cr is the only metallic element in $M_{23}C_6$ and M_7C_3. The unit cell of $Cr_{23}C_6$ contains 92 chromium atoms and 24 carbon atoms with the volume of 1.19 nm^3 [57] and the unit cell of Cr_7C_3 contains 28 chromium atoms and 12 carbon atoms with the volume of 0.38 nm^3 [58]. Assuming the transformation is controlled by the diffusion of chromium atoms and that the number of carbon atoms within the carbide is constant, the volume of the Cr_7C_3 carbide is expected to increase by about 56 % when it transforms into $Cr_{23}C_6$. On the other hand, if the $M_7C_3 \rightarrow M_{23}C_6$ transformation is controlled by the diffusion of carbon atoms while the number of chromium atoms remain unchanged. The carbide volume would be expected to shrink by less than 5% upon the transformation from M_7C_3 to $M_{23}C_6$.

To determine the primary carbide volume change during the transformation, the equivalent sizes of 50 partially transformed M_7C_3 - $M_{23}C_6$ carbides were measured for each heat-treated sample. The total area of partially transformed primary carbide and the area of the remaining M_7C_3 core were firstly measured as shown in Figure 9 (a) and the area was considered to be equivalent to a circular

area. Then equivalent sizes of the carbide and the remaining M_7C_3 core are deduced based on $A=\pi r^2$ and the difference between these two equivalent sizes is the shell thickness of $M_{23}C_6$, as shown in Figure 9 (b). The results are summarized in Table 3. It can be seen that the M_7C_3 carbide size continuously decreases with the increasing heat treatment time, as expected. The averaged total size of the primary carbide is approximately constant (2.2 μm - 2.4 μm). This indicates that the size and therefore the volume of the primary carbide remain similar during the $M_7C_3 \rightarrow M_{23}C_6$ transformation, which is close to the scenario if the transformation is controlled by the diffusion of carbon atoms (i.e. less than 5% volume change).

The growth rate of $M_{23}C_6$ could also be estimated based on Zener's empirical relation [59] where the diffusion controlled growth can be expressed as $r = \sqrt{2Dt}$, with r being the radius of the growing object, D the diffusion coefficient and t the time. At 1000 ^{o}C, carbon diffusion coefficient in $M_{23}C_6$ is about 2.72×10^{-17} m^2/s [60] and chromium diffusion coefficient in $M_{23}C_6$ is however a few orders of magnitude slow at about 9.16×10^{-23} m^2/s [61]. Figure 10 compares the $M_{23}C_6$ shell thickness calculated from Zener's empirical relation with the equivalent $M_{23}C_6$ shell thickness determined from the current study. The estimated diffusion distance of carbon in $M_{23}C_6$ agrees reasonably well with the $M_{23}C_6$ growth rate while the diffusion distance of chromium in $M_{23}C_6$ is much smaller than the measured thickness. Therefore, it is likely that the $M_7C_3 \rightarrow M_{23}C_6$ transformation is controlled by the diffusion of the carbon from M_7C_3 to the matrix through the $M_{23}C_6$ shell, following its natural concentration gradient, rather than the uphill diffusion of Cr from the matrix into the M_7C_3.

The M_7C_3 to $M_{23}C_6$ transformation is shown schematically in Figure 11. At the beginning of this transformation, the $M_{23}C_6$ nucleates at the M_7C_3-matrix interface. The nucleated $M_{23}C_6$ carbide is coherent with the austenitic matrix and forms a shell surrounding the original M_7C_3 carbide. The $M_{23}C_6$ carbide grows into the M_7C_3, mainly controlled by the diffusion of carbon through $M_{23}C_6$ to the matrix until the transformation completes. A precipitation free zone (PFZ) can be identified around the

primary carbide, as shown in Figure 11(c) obtained from the sample after 5 hours heat-treatment. However, as noted in Figure 2(c) a Cr concentration trough exists in the matrix next to the primary M_7C_3 carbides in the as-cast alloy. Indeed, it has been found (not shown here) that the Cr concentration trough gradually disappeared with the prolonged heat-treatment. At low Cr concentration, secondary chromium carbide precipitation would be suppressed. In other words, the PFZ observed is a consequence of the local Cr content in the region next to the primary carbides, which was probably caused during the solidification process.

Conclusions

1. The microstructure of the as-cast HP-MA consists of austenitic matrix surrounded by a primary carbide network consisting of M_7C_3 and MC, formed during the fast solidification.

2. After heat treatment at 1000 ^{o}C, the Cr-rich primary carbides transformed from M_7C_3 to $M_{23}C_6$, forming a core-shell structure. EBSD mapping and TEM analysis confirmed that the outside shell is $M_{23}C_6$ carbide having the same orientation as the austenite matrix and that the core is M_7C_3 carbide.

3. It is envisaged that during the $M_7C_3 \rightarrow M_{23}C_6$ transformation, $M_{23}C_6$ nucleates at the M_7C_3-matrix interface and forms a shell around the original M_7C_3 precipitates. The $M_{23}C_6$ grows continually inward into the M_7C_3. The kinetics of the transformation is likely controlled by the diffusion of carbon through the $M_{23}C_6$.

Acknowledgement

The authors wish to acknowledge the support from the Doncasters Group Ltd. The research has benefitted from the access to facilities funded Engineering and Physical Science Research Council (EP/L017725/1) of the UK.

References

1. Kalamaras, C.M. and A.M. Efstathiou, *Hydrogen production technologies: current state and future developments*, in *Power options for the eastern mediterrancean region*. 2013, Hindawi Publishing Corporation: Limassol, Cyprus. p. 9.
2. Abbas, H.F. and W.W. Daud, *Hydrogen production by methane decomposition: A review.* International Journal of Hydrogen Energy, 2010. **35**(3): p. 1160-1190.
3. Ayabe, S., H. Omoto, T. Utaka, R. Kikuchi, K. Sasaki, Y. Teraoka, and K. Eguchi, *Catalytic autothermal reforming of methane and propane over supported metal catalysts.* Applied Catalysis A-General, 2003. **241**(1-2): p. 261-269.
4. Rakib, M.A., J.R. Grace, C.J. Lim, S.H. Elnashaie, and B. Ghiasi, *Steam reforming of propane in a fluidized bed membrane reactor for hydrogen production.* International Journal of Hydrogen Energy, 2010. **35**(12): p. 6276-6290.
5. Pino, L., V. Recupero, S. Beninati, A.K. Shukla, M.S. Hegde, and P. Bera, *Catalytic partial-oxidation of methane on a ceria-supported platinum catalyst for application in fuel cell electric vehicles.* Applied Catalysis A-General, 2002. **225**(1-2): p. 63-75.
6. LeValley, T.L., A.R. Richard, and M.H. Fan, *The progress in water gas shift and steam reforming hydrogen production technologies - A review.* International Journal of Hydrogen Energy, 2014. **39**(30): p. 16983-17000.
7. Edeleanu, C., *Materials Technology in Steam Reforming Processes: Proceedings*. 1966: Symposium Publications Division, Pergamon Press.
8. Hou, W.T. and R.W.K. Honeycombe, *Structure of Centrifugally Cast Austenitic Stainless-Steels .1. Hk-40 as Cast and after Creep between 750 ^{o}C and 1000 ^{o}C.* Materials Science and Technology, 1985. **1**(5): p. 385-389.
9. Hou, W.T. and R.W.K. Honeycombe, *Structure of Centrifugally Cast Austenitic Stainless-Steels .2. Effects of Nb, Ti, and Zr.* Materials Science and Technology, 1985. **1**(5): p. 390-397.
10. Ibanez, R.P., G.D. Soares, L.H. Dealmeida, and I. Lemay, *Effects of Si Content on the Microstructure of Modified-HP Austenitic Steels.* Materials Characterization, 1993. **30**(4): p. 243-249.
11. Kuzucu, V., M. Aksoy, and M.H. Korkut, *The effect of strong carbide-forming elements such as Mo, Ti, V and Nb on the microstructure of ferritic stainless steel.* Journal of Materials Processing Technology, 1998. **82**(1-3): p. 165-171.
12. de Almeida, L.H., A.F. Ribeiro, and I. Le May, *Microstructural characterization of modified 25Cr-35Ni centrifugally cast steel furnace tubes.* Materials Characterization, 2002. **49**(3): p. 219-229.
13. Barbabela, G.D., Almeida, L.H., Silveira, T.L., Le May, I., *Role of Nb in modifying the microstructure of heat-resistant cast HP steel*, Materials Characterization, 1991. **26**, Pages 193-197.
14. Yan, J.B., Y.M. Gao, F. Yang, C.Y. Yao, Z.Z. Ye, D.W. Yi, and S.Q. Ma, *Effect of tungsten on the microstructure evolution and mechanical properties of yttrium modified HP40Nb alloy.* Materials Science and Engineering A-Structural Materials Properties Microstructure and Processing, 2011. **529**: p. 361-369.
15. Nunes, F.C., L.H. de Almeida, J. Dille, J.L. Delplancke, and I. Le May, *Microstructural changes caused by yttrium addition to NbTi-modified centrifugally cast HP-type stainless steels.* Materials Characterization, 2007. **58**(2): p. 132-142.
16. Nunes, F.C., J. Dille, J.L. Delplancke, and L.H. de Almeida, *Yttrium addition to heat-resistant cast stainless steel.* Scripta Materialia, 2006. **54**(9): p. 1553-1556.

17. Cho, B., S. Chung, K. Kim, T. Kang, C. Park, and B. Kim, *Photoemission study of the stainless steel surface interacting with oxygen.* Applied Surface Science, 2001. **173**(1-2): p. 22-29.
18. Wiengmoon, A., *Carbides in High Chromium Cast Irons*. 2011.
19. Goldschmidt, H.J., *Interstitial alloys*. 1967: Plenum Press.
20. West, D.F. and N. Saunders, *Ternary Phase Diagrams in Materials Science*. 2002: Maney for the Institute of Materials.
21. Adamson, J.P. and J.W. Martin, *Nucleation of $M_{23}C_6$ Carbide Particles in Grain Boundaries of an Austenitic Stainless Steel.* Acta Metallurgica, 1971. **19**(10): p. 1015-1018.
22. Carolan, R.A. and R.G. Faulkner, *Grain-Boundary Precipitation of $M_{23}C_6$ in an Austenitic Steel.* Acta Metallurgica, 1988. **36**(2): p. 257-266.
23. Stickler, R. and A. Vinckier, *Morphology of Grain Boundary Carbides in a 304 Stainless Steel.* Acta Metallurgica, 1961. **9**(9): p. 898-899.
24. Beckitt, F.R. and B.R. Clark, *Shape and Mechanism of Formation of $M_{23}C_6$ Carbide in Austenite.* Acta Metallurgica, 1967. **15**(1): p. 113-129.
25. Terao, N. and B. Sasmal, *Precipitation of $M_{23}C_6$ Type Carbide on Twin Boundaries in Austenitic Stainless-Steels.* Metallography, 1980. **13**(2): p. 117-133.
26. Kirchheiner, R. and P. Woelpert, *Niobium in centrifugally cast tubes for petrochemical applications.* Niobium: Science & Technology, 2001: p. 1041-1054.
27. Soares, G.D., L.H. Dealmeida, T.L. Dasilveira, and I. Lemay, *Niobium Additions in HP Heat-Resistant Cast Stainless-Steels.* Materials Characterization, 1992. **29**(4): p. 387-396.
28. Yan, J.B., Y.M. Gao, L. Liang, Z.Z. Ye, Y.F. Li, W. Chen, and J.J. Zhang, *Effect of yttrium on the cyclic oxidation behaviour of HP40 heat-resistant steel at 1373 K.* Corrosion Science, 2011. **53**(1): p. 329-337.
29. Wiengmoon, A., T. Chairuangsri, A. Brown, R. Brydson, D.V. Edmonds, and J.T.H. Pearce, *Microstructural and crystallographical study of carbides in 30wt.%Cr cast irons.* Acta Materialia, 2005. **53**(15): p. 4143-4154.
30. Imurai, S., C. Thanachayanont, J.T.H. Pearce, K. Tsuda, and T. Chairuangsri, *Effects of Mo on microstructure of as-cast 28 wt.% Cr-2.6 wt.% C-(0-10) wt.% Mo irons.* Materials Characterization, 2014. **90**: p. 99-112.
31. Vardavoulias, M., G. Papadimitriou, and D. Pantelis, *Effect of M_7C_3-$M_{23}C_6$ Transformation on Fracture-Behavior of Cast Ferritic Stainless-Steels.* Materials Science and Technology, 1993. **9**(8): p. 711-717.
32. Wiengmoon, A., T. Chairuangsri, and J.T.H. Pearce, *A microstructural study of destabilised 30wt%Cr-2.3wt%C high chromium cast iron.* ISIJ International, 2004. **44**(2): p. 396-403.
33. Jiang, W.H., X.D. Yao, H.R. Guan, and Z.Q. Hu, *Relationship between degeneration of M_7C_3 and precipitation of $M_{23}C_6$ in a cobalt base superalloy.* Materials Science and Technology, 1999. **15**(5): p. 596-598.
34. Inoue, A. and T. Masumoto, *Carbide Reactions M_3C-M_7C_3-$M_{23}C_6$-M_6C during Tempering Of Rapidly Solidified High-Carbon Cr-W And Cr-Mo Steels.* Metallurgical Transactions A-Physical Metallurgy And Materials Science, 1980. **11**(5): p. 739-747.
35. Wieczerzak, K., P. Bala, R. Dziurka, T. Tokarski, G. Cios, T. Koziel, and L. Gondek, *The effect of temperature on the evolution of eutectic carbides and M_7C_3 -> $M_{23}C_6$ carbides reaction in the rapidly solidified Fe-Cr-C alloy.* Journal of Alloys and Compounds, 2017. **698**: p. 673-684.
36. Ernst, F., D.Q. Li, H. Kahn, G.M. Michal, and A.H. Heuer, *The carbide M_7C_3 in low-temperature-carburized austenitic stainless steel.* Acta Materialia, 2011. **59**(6): p. 2268-2276.
37. Bondar, A., V. Ivanchenko, A. Kozlov, and J.-C. Tedenac, *Carbon – Chromium – Iron: Datasheet from Landolt-Börnstein - Group IV Physical Chemistry · Volume 11D2: "Iron Systems, Part 2" in SpringerMaterials (https://dx.doi.org/10.1007/978-3-540-74196-1_3)*. Springer-Verlag Berlin Heidelberg.

38. Vyrostkova, A., A. Kroupa, J. Janovec, and M. Svoboda, *Carbide reactions and phase equilibria in low alloy Cr-Mo-V steels tempered at 773-993 K. Part I: Experimental measurements.* Acta Materialia, 1998. **46**(1): p. 31-38.
39. Fan, C., M.C. Chen, C.M. Chang, and W.T. Wu, *Microstructure change caused by $(Cr,Fe)_{23}C_6$ carbides in high chromium Fe-Cr-C hardfacing alloys.* Surface & Coatings Technology, 2006. **201**(3-4): p. 908-912.
40. Gregolin, J.R. and N.G. Alcantara, *Solidification and Phase-Equilibria in the Fe-C-Cr-NbC System.* Metallurgical Transactions A-Physical Metallurgy and Materials Science, 1991. **22**(10): p. 2181-2186.
41. Marshall, P., *Austenitic Stainless Steels: Microstructure and mechanical properties*. 1984: Springer Netherlands.
42. Wieczerzak, K., P. Bala, M. Stepien, G. Cios, and T. Koziel, *Formation of eutectic carbides in Fe-Cr-Mo-C alloy during non-equilibrium crystallization.* Materials & Design, 2016. **94**: p. 61-68.
43. Hall, E.L. and C.L. Briant, *Chromium Depletion in the Vicinity of Carbides in Sensitized Austenitic Stainless-Steels.* Metallurgical Transactions A-Physical Metallurgy and Materials Science, 1984. **15**(5): p. 793-811.
44. Yin, Y.F., R.G. Faulkner, P. Moreton, I. Armson, and P. Coyle, *Grain boundary chromium depletion in austenitic alloys.* Journal of Materials Science, 2010. **45**(21): p. 5872-5882.
45. Kai, J.J. and M.N. Liu, *The Effects of Heat-Treatment on the Carbide Evolution and the Chromium Depletion Along Grain-Boundary of Inconel-690 Alloy.* Scripta Metallurgica, 1989. **23**(1): p. 17-22.
46. Honeycombe, R.W., H.H. Bhadeshia, and H. Bhadeshia, *Steels: Microstructure and Properties*. 1995: E. Arnold.
47. Benz, R., J.F. Elliott, and J. Chipman, *Thermodynamics of Carbides in System Fe-Cr-C.* Metallurgical Transactions, 1974. **5**(10): p. 2235-2240.
48. Barbabela, G.D., L.H. Dealmeida, T.L. Dasilveira, and I. Lemay, *Role of Nb in Modifying the Microstructure of Heat-Resistant Cast HP Steel.* Materials Characterization, 1991. **26**(3): p. 193-197.
49. Barbabela, G.D., L.H. Dealmeida, T.L. Dasilveira, and I. Lemay, *Phase Characterization in two Centrifugally Cast HK Stainless-Steel Tubes.* Materials Characterization, 1991. **26**(1): p. 1-7.
50. Kaneko, K., T. Fukunaga, K. Yamada, N. Nakada, M. Kikuchi, Z. Saghi, J.S. Barnard, and P.A. Midgley, *Formation of $M_{23}C_6$-type precipitates and chromium-depleted zones in austenite stainless steel.* Scripta Materialia, 2011. **65**(6): p. 509-512.
51. Hong, H.U., B.S. Rho, and S.W. Nam, *Correlation of the $M_{23}C_6$ precipitation morphology with grain boundary characteristics in austenitic stainless steel.* Materials Science and Engineering A-Structural Materials Properties Microstructure and Processing, 2001. **318**(1-2): p. 285-292.
52. Kittel, C., *Introduction to Solid State Physics*. 2005: Wiley.
53. Xie, J.Y., N. Chen, L.D. Teng, and S. Seetharaman, *Atomistic study on the site preference and thermodynamic properties for $Cr_{23-x}Fe_xC_6$.* Acta Materialia, 2005. **53**(20): p. 5305-5312.
54. Henriksson, K.O.E., N. Sandberg, and J. Wallenius, *Carbides in stainless steels: Results from ab initio investigations.* Applied Physics Letters, 2008. **93**(19).
55. Baltusnikas, A., I. Lukosiute, V. Makarevicius, R. Kriukiene, and A. Grybenas, *Influence of Thermal Exposure on Structural Changes of $M_{23}C_6$ Carbide in P91 Steel.* Journal of Materials Engineering and Performance, 2016. **25**(5): p. 1945-1951.
56. Litasov, K.D., S.V. Rashchenko, A.N. Shmakov, Y.N. Palyanov, and A.G. Sokol, *Thermal expansion of iron carbides, Fe_7C_3 and Fe_3C, at 297-911 K determined by in situ X-ray diffraction.* Journal of Alloys and Compounds, 2015. **628**: p. 102-106.

57. Yakel, H.L., *Atom Distributions in Tau Carbide Phases - Fe and Cr Distributions in ($Cr_{23-x}Fe_x)C_6$ with x=0, 0.74, 1.70, 4.13 and 7.36.* Acta Crystallographica Section B-Structural Science, 1987. **43**: p. 230-238.
58. Rouault, M.A., P. Herpin, and M.R. Fruchart, *Crystallographic Study of Carbides Cr_7C_3 and Mn_7C_3.* Annales De Chimie France, 1970. **5**(6): p. 461-470.
59. Sahlaoui, H., H. Sidhom, and J. Philibert, *Prediction of chromium depleted-zone evolution during aging of Ni-Cr-Fe alloys.* Acta Materialia, 2002. **50**(6): p. 1383-1392.
60. Mayr, W., W. Lengauer, P. Ettmayer, D. Rafaja, J. Bauer, and M. Bohn, *Phase equilibria and multiphase reaction diffusion in the Cr-C and Cr-N systems.* Journal of Phase Equilibria, 1999. **20**(1): p. 35-44.
61. Wang, M., *Microstructure characterisation and creep modelling of HP40 alloys*. 2017, University of Birmingham: PhD thesis.

421 Table 1 The chemical composition of the as-cast HP-MA determined by optical emission spectrometry

Elements	C	Si	Mn	Ni	Cr	Mo	Nb	Ti	Zr	Fe
wt %	0.41	0.92	0.75	36.12	23.49	0.02	1.39	0.05	0.01	36.84

422

423 Table 2 EDS analysis results obtained from as-cast HP-MA and HT-5 HP-MA.

Elements / at %	As-cast			HT-5
	Matrix	MC	M_7C_3	$M_{23}C_6$
C	---	51.08±0.52	31.85±0.72	21.67±1.21
Si	2.13±0.35	---	---	---
Cr	25.25±0.91	---	59.63±1.13	61.64±0.84
Fe	37.50±1.01	---	7.30±0.68	11.17±0.39
Ni	34.23±0.53	---	1.21±0.22	4.84±0.47
Mn	0.89±0.13	---	0.59±0.02	0.68±0.20
Nb	---	47.58±0.69	---	---
Ti	---	1.35±0.51	---	---

424

425 Table 3 Measured areas and equivalent sizes of Cr-carbides and $M_{23}C_6$ shell thickness in the heat-

426 treated HP-MA samples.

Specimen	Measured area / μm^2		Equivalent size / μm		$M_{23}C_6$ shell thickness / μm
	Total	M_7C_3	Total	M_7C_3	
HT-1	20.29 ± 13.21	11.83 ± 8.28	2.40 ± 0.83	1.8 ± 0.72	0.60 ± 0.31
HT–3	20.59 ± 12.31	9.82 ± 7.13	2.45 ± 0.76	1.65 ± 0.63	0.80 ± 0.28
HT-5	16.75 ± 9.09	4.99 ± 3.83	2.23 ± 0.63	1.17 ± 0.48	1.06 ± 0.39
HT-7	17.15 ± 10.68	4.07 ± 3.52	2.24 ± 0.68	1.05 ± 0.45	1.19 ± 0.49
HT-9	19.14 ± 11.61	3.73 ± 3.02	2.36 ± 0.72	1.00 ± 0.43	1.36 ± 0.41

427

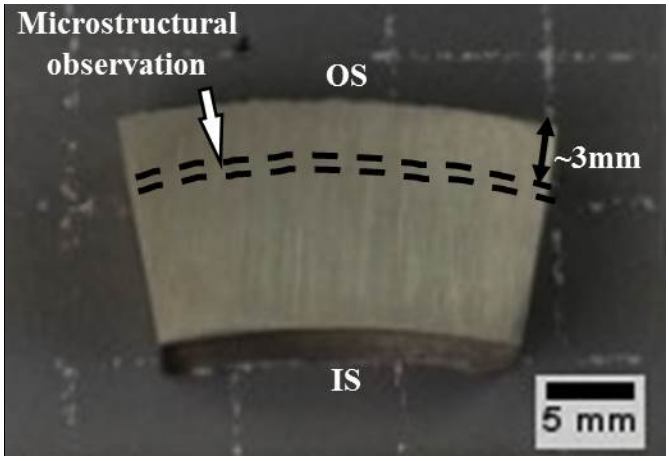

428

429 Figure 1. Optical image of a section of the HP-MA tube. The region between the dashed lines was

430 used for microstructural observation.

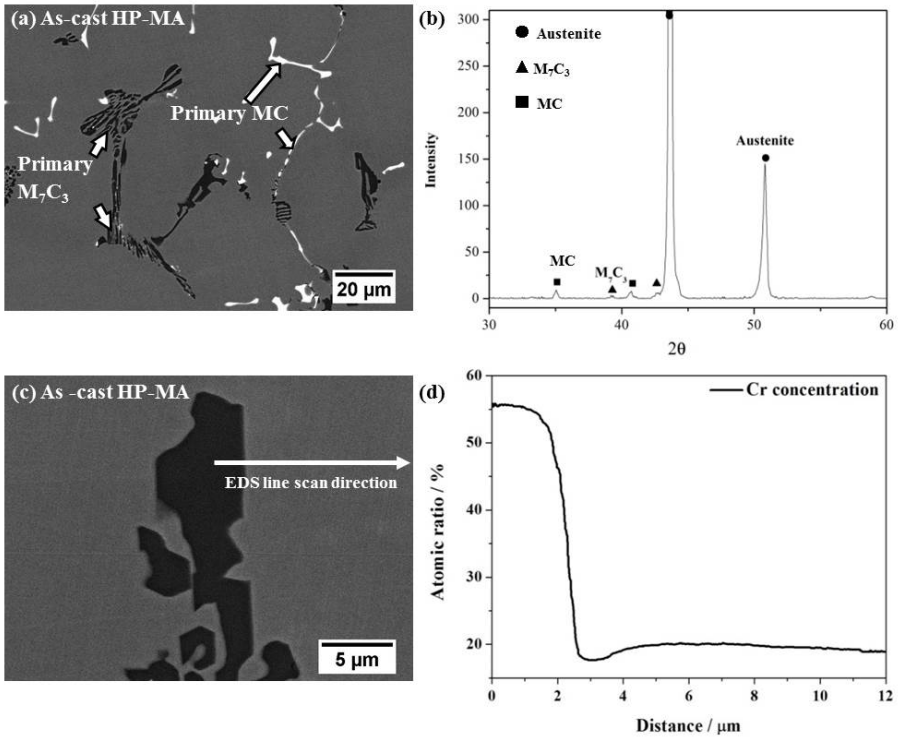

431

432 Figure 2. (a) BSE image of the as-cast HP-MA illustrating primary carbides of Cr-rich M_7C_3 type and

433 Nb-rich MC type; (b) XRD spectrum obtained from the as-cast HP-MA illustrating that the primary

434 carbides are M_7C_3 and MC; (c) BSE image of the primary Cr-rich carbide in the as-cast HP-MA; (d)

435 EDS line scan obtained from the position shown in (c) indicating the depletion of Cr in the matrix

436 close to the primary carbide.

437

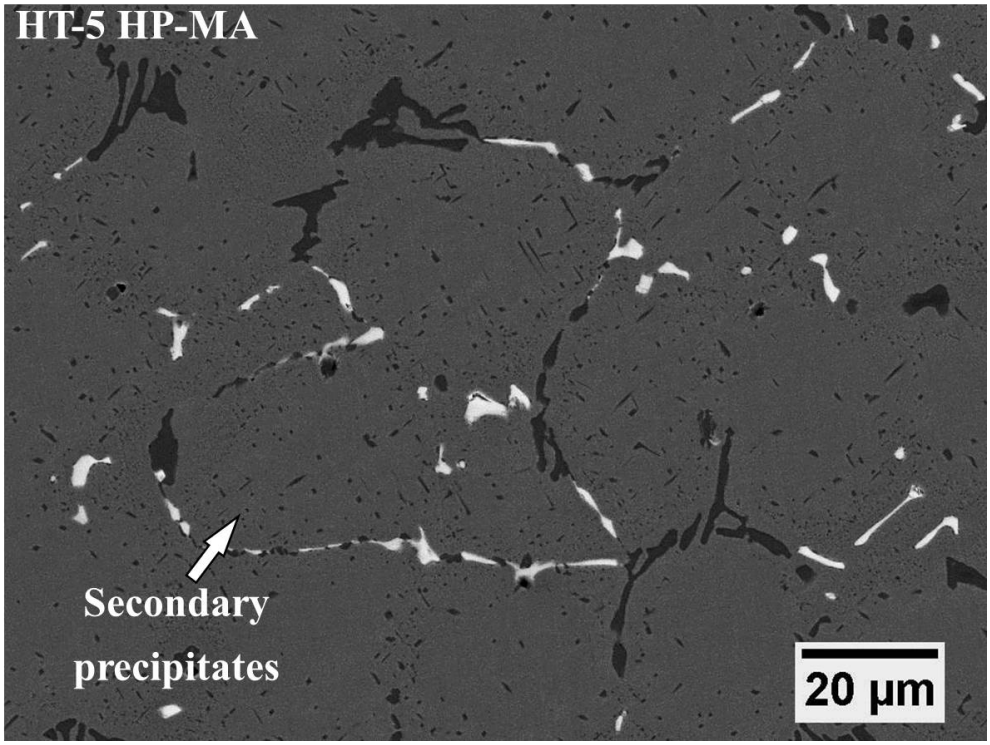

Figure 3. BSE image showing the secondary carbides formed in the HT-5 HP-MA sample.

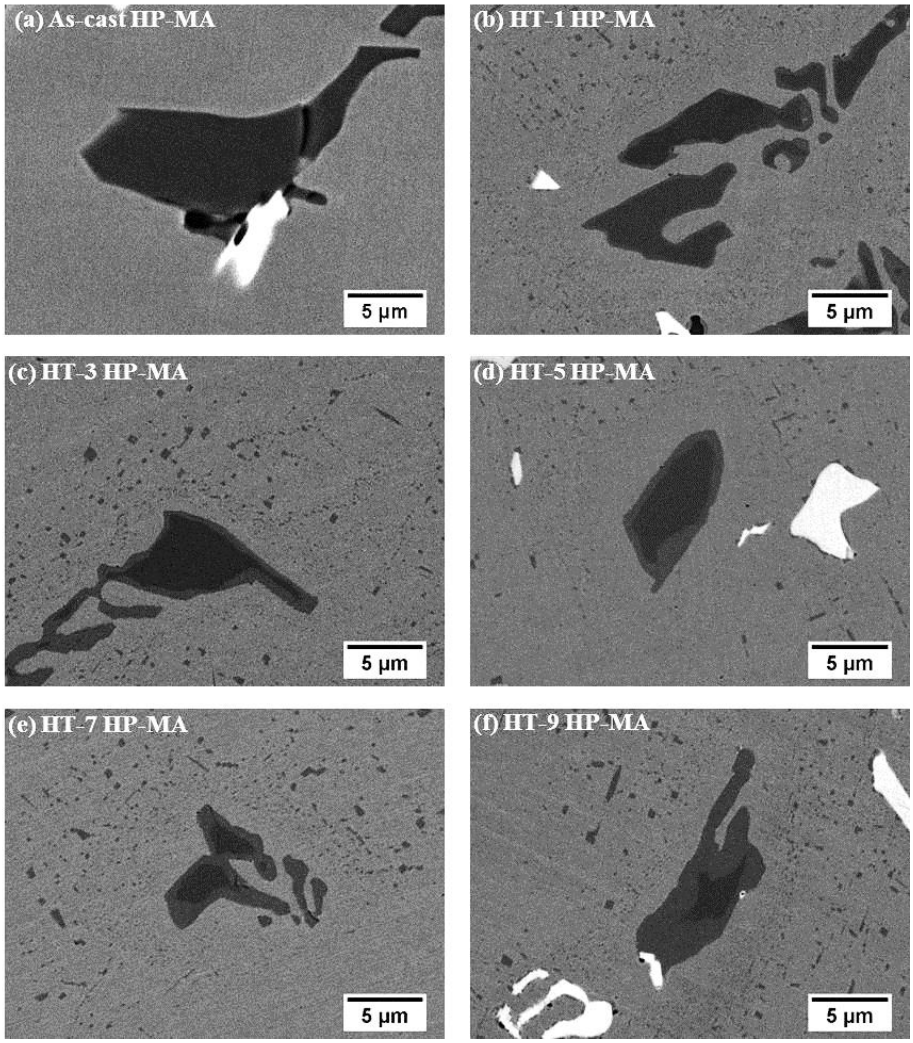

442

443 Figure 4. SEM BSE images obtained from the as-cast (a) and the heat-treated HP-MA samples after
444 the heat-treatment at 1000 ^{o}C for 1h-9h (b-f) illustrating that the primary Cr-carbides have two grey
445 levels of contrast.

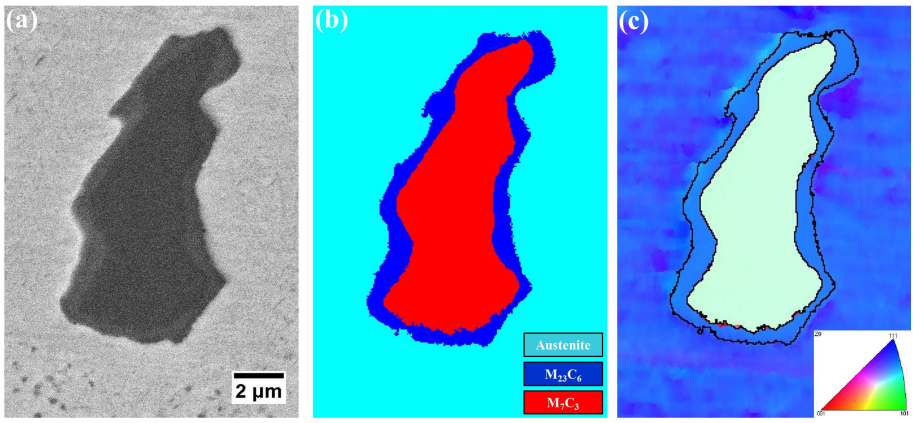

Figure 5. (a) A BSE imaged obtained from a Cr-rich primary carbide in the HT-5 HP-MA sample. The EBSD phase map (b) illustrates that the outside shell of the particle is of $M_{23}C_6$ structure and that the core is of M_7C_3; (c) the colour-coded orientation map shows that the $M_{23}C_6$ shell has the same orientation as that of the surrounding matrix.

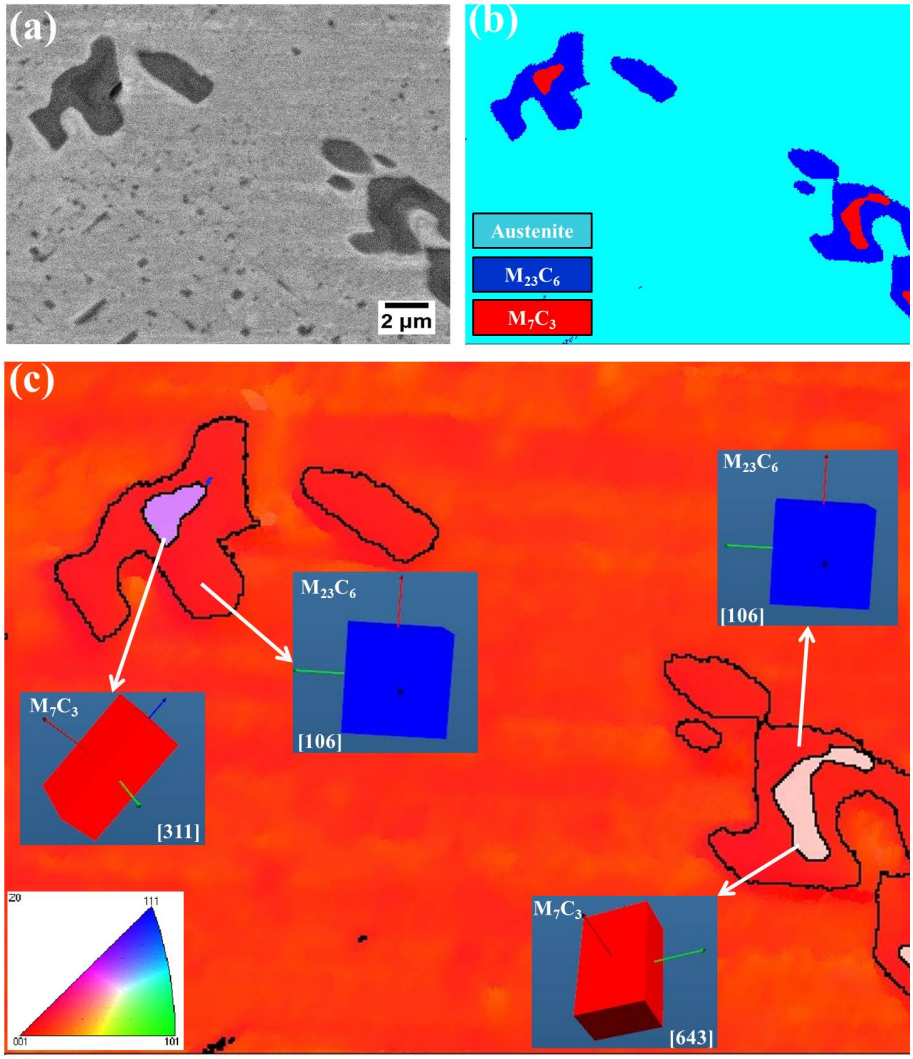

Figure 6. (a) A BSE image and (b) a phase map showing Cr-rich primary carbides in a HT-5 HP-MA sample; the colour-coded orientation map (c) illustrates that all the $M_{23}C_6$ shells have the same orientation as the matrix while the M_7C_3 cores have two different orientations

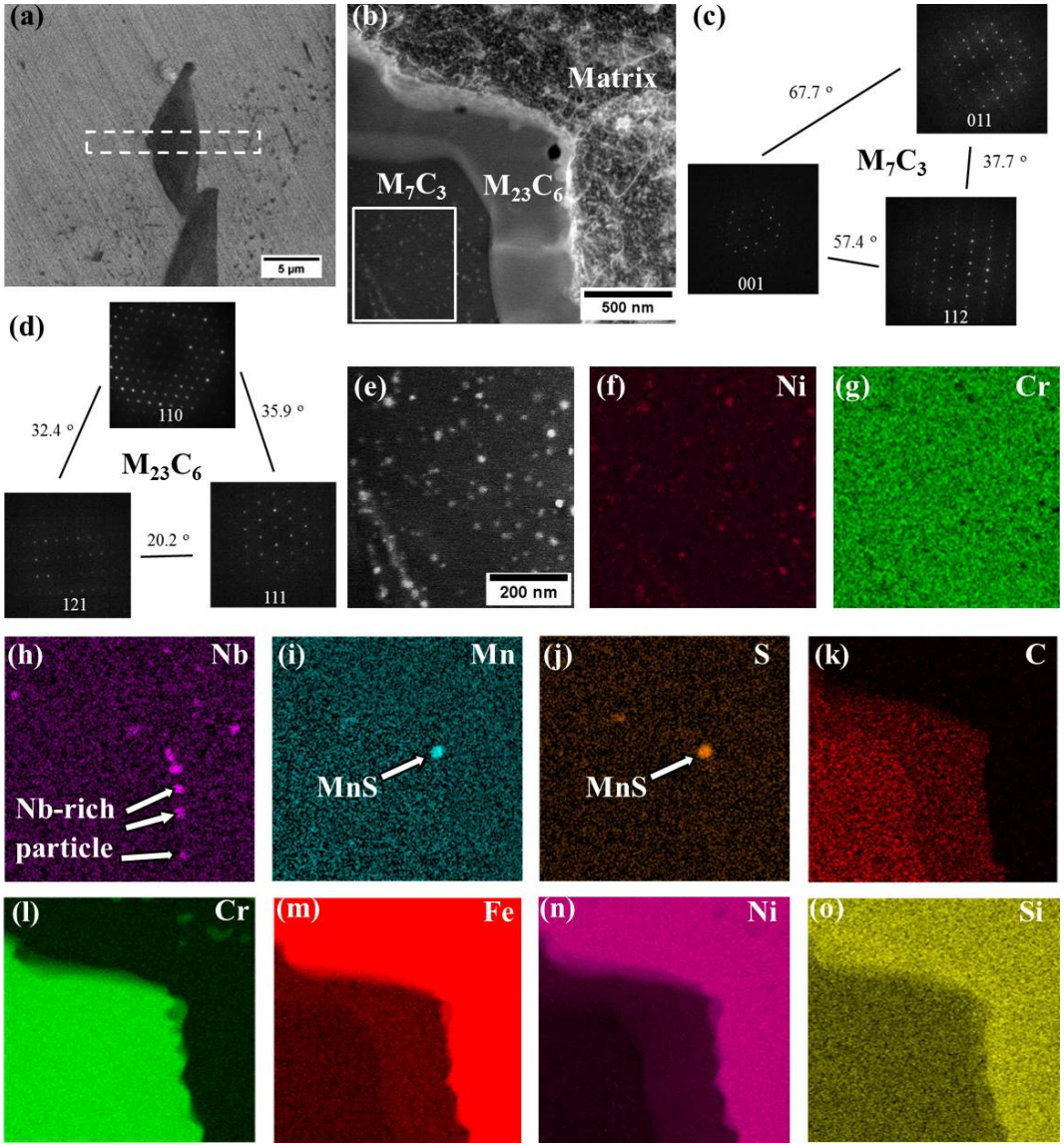

Figure 7 (a) An SEM BSE image showning a Cr-rich primary carbide in the HT-5 HP-MA sample where a TEM foil was extracted from. The dashed rectrangle shows the position where the foil was extracted. (b) The TEM BF image obtained from the FIB-extracted foil; Diffraction patterns obtained from (c) the M_7C_3 core and (d) the $M_{23}C_6$ shell. A higher magnficantion BF image (e) was obtained from the region enclosed by the rectangle in (b) and the corresponding quantitative EDS maps (at%) are shown in (e-g). (f) Illustrates small particles are rich in Ni; (h-o) quantitative EDS maps (at%) for the whole region in (b). (h) Nb-rich particles; (i)&(j) MnS particle were observed at the interface between the $M_{23}C_6$ shell and the matrix; (k) the carbon elemental map shows that the concentration of carbon is the highest in M_7C_3 followed by that in $M_{23}C_6$ and the lowest in the surrounding matrix; The

Cr map (l) shows similar contrast from the M_7C_3 core and the $M_{23}C_6$ shell; (m) and (n) illustrate that $M_{23}C_6$ contains more Fe and Ni than M_7C_3 and (o) Si is mostly present in the austenitic matrix

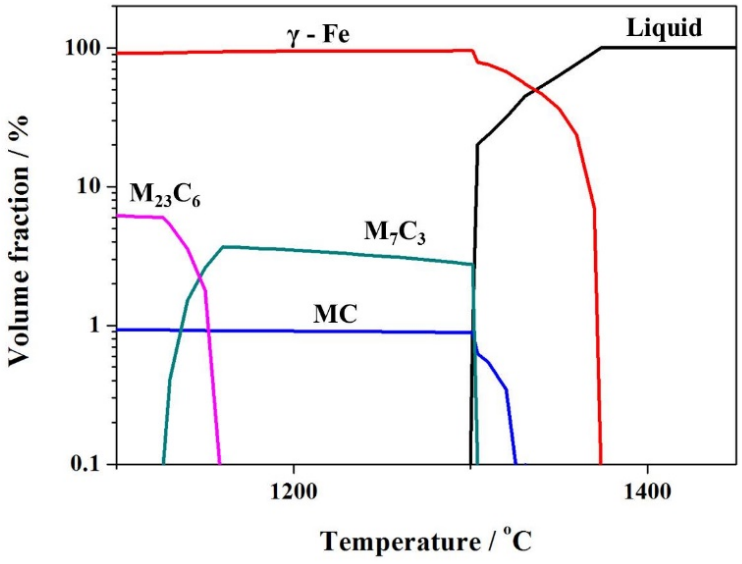

Figure 8 The equilibrium phases expected in the HP-MA steel according to JMat Pro.

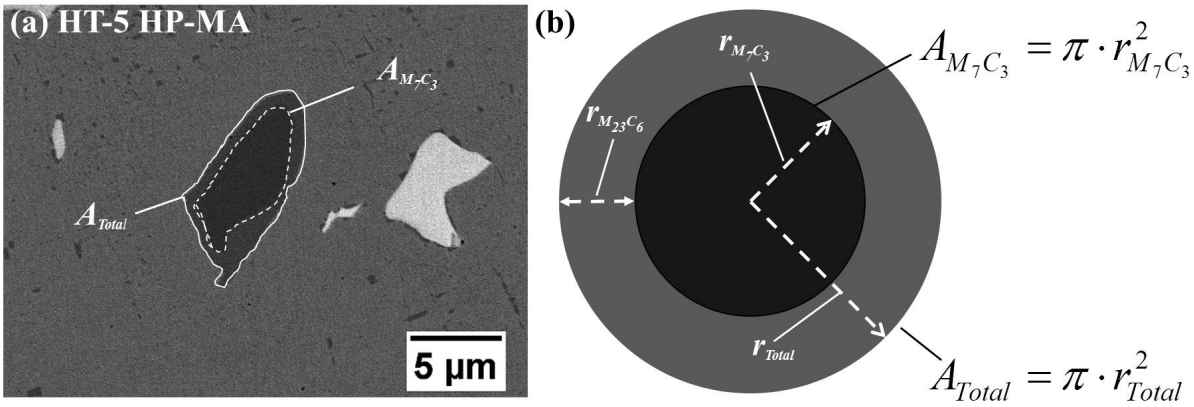

Figure 9 An example showing the measurement of the total area of the M_7C_3-$M_{23}C_6$ carbide (enclosed by the solid line) and the area of M_7C_3 (enclosed by the dashed line) in the HT-5 HP-MA sample; (b) Two circles of the same areas as that of the total M_7C_3-$M_{23}C_6$ carbide area and that of the M_7C_3 area are shown in (b). The corresponding radii of the circles (r_{Total} and $r_{M_7C_3}$) and the thickness of the $M_{23}C_6$ shell could be determined.

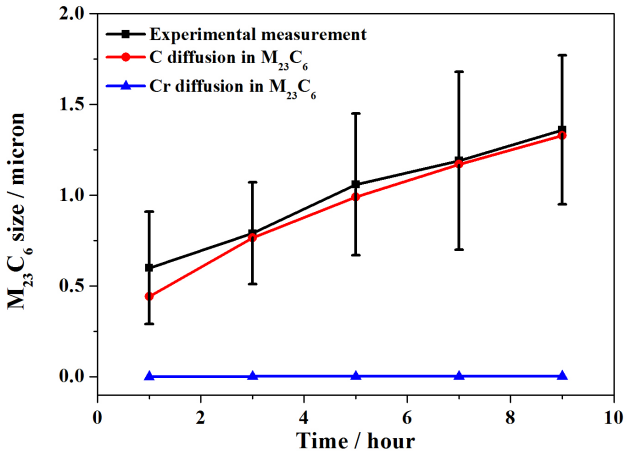

478

479 Figure 10 The experimentally determined $M_{23}C_6$ shell thickness was plotted against the heat-treatment

480 time at 1000 °C, together with the estimated diffusion distances of Cr and C in $M_{23}C_6$ (see text for

481 details), following equation $r = \sqrt{2Dt}$.

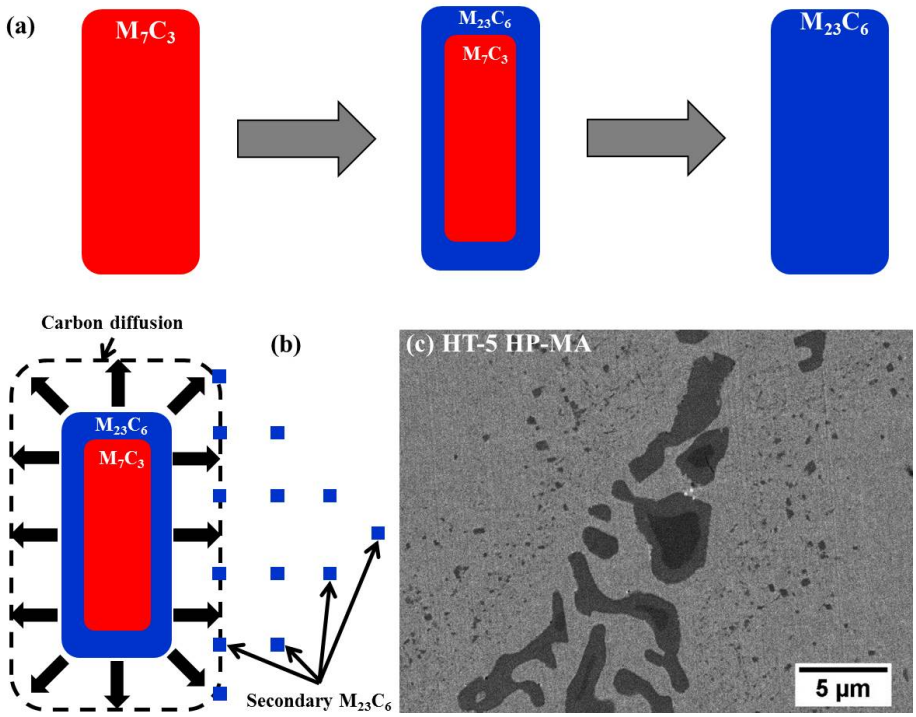

482

483 Figure 11 (a) Schematic diagrams illustrating the transformation from M_7C_3 to $M_{23}C_6$. The release of

484 carbon occurred during the $M_7C_3 \rightarrow M_{23}C_6$ transformation is expected to promote the precipitation of

485 $M_{23}C_6$ secondary carbide close to the primary carbide, as illurstated in (b), which is consistent with the

486 experimental observation as examplified in (c) obtained from the sample after 5 hours heat-treatment.